nature biomedical engineering

ARTICLES

https://doi.org/10.1038/s41551-021-00763-4

Check for updates

Continuous monitoring of deep-tissue haemodynamics with stretchable ultrasonic phased arrays

Chonghe Wang[1,9,10], Baiyan Qi[2,10], Muyang Lin[1,10], Zhuorui Zhang[1,10], Mitsutoshi Makihata[1], Boyu Liu[1], Sai Zhou[1], Yi-hsi Huang[1], Hongjie Hu[2], Yue Gu[2], Yimu Chen[1], Yusheng Lei[1], Taeyoon Lee[3,4], Shu Chien[5], Kyung-In Jang[6], Erik B. Kistler[5,7] and Sheng Xu[1,2,5,8] ✉

Stretchable wearable devices for the continuous monitoring of physiological signals from deep tissues are constrained by the depth of signal penetration and by difficulties in resolving signals from specific tissues. Here, we report the development and testing of a prototype skin-conformal ultrasonic phased array for the monitoring of haemodynamic signals from tissues up to 14 cm beneath the skin. The device allows for active focusing and steering of ultrasound beams over a range of incident angles so as to target regions of interest. In healthy volunteers, we show that the phased array can be used to monitor Doppler spectra from cardiac tissues, record central blood flow waveforms and estimate cerebral blood supply in real time. Stretchable and conformal skin-worn ultrasonic phased arrays may open up opportunities for wearable diagnostics.

Most chronic diseases directly manifest on one or more deep tissues[1]. Thus, continuous and non-invasive monitoring of physiological signals in deep tissues to interrogate disease initiation and progression is paramount to support clinical decisions for diagnosing and treating chronic diseases[2,3]. However, two major characteristics of deep tissues present challenges to continuous and non-invasive signal acquisition (Fig. 1a). First, they are buried under strongly attenuating tissue layers[4]. Second, object dimensions range from decimetres to micrometres. Therefore, to capture biological parameters in deep tissues of interest, measurement strategies must possess both sufficient penetration depth and high spatial resolution. At present, clinically available imaging techniques that can achieve both, including X-ray computed tomography, magnetic resonance imaging and positron emission tomography, are widely used by trained practitioners. However, due in part to their large footprint and high cost, these modalities are generally only accessible at a tertiary hospital or clinic. There is a critical need for continuous and non-invasive monitoring of anatomies and functions deep beneath the skin surface in both in- and outpatient environments.

Stretchable electronics that place a minimum constraint on the motion of the participant provide an exciting avenue for continuous and non-invasive monitoring of patient conditions[5–7]. Considerable efforts have been expended to overcome the challenges of probing deep tissues with stretchable electronics (Extended Data Fig. 1). Sensing modalities based on optical[8–10], thermal[11,12], chemical[5,13], terahertz[14–16] and radiofrequency[4] mechanisms lack either penetration depth or spatial resolution. Ultrasonic waves have remarkable penetration depth in—and proven biocompatibility with—the human tissues. An unfocused single element has a penetration depth of ~3–4 cm and can sense a region directly beneath it (also known as line-of-sight detection)[17,18]. Considering the complexity of human anatomy[19], it is very challenging to target specific regions with a single element. The phased-array technique, which synchronizes an array of transducers to enhance the energy density and enable beam steering, is ideal for overcoming this challenge[20–22]. Some cell phone-based ultrasound phased arrays can provide accurate diagnoses by clinicians and show great promise, as well as developing trends in the field (for example, https://www.butterflynetwork.com/iq, https://www.usa.philips.com/healthcare/sites/lumify and https://www.sonoque.com/)[23], but these commercial machines are more in the realm of accessibility rather than advancements in technology per se. Also, they are still on rigid substrates with thick profiles[24–27] and require burdensome manual holding during measurements, which precludes them from unobtrusive integration with the human body for continuous and long-term monitoring. There are some efforts on flexible phased arrays that can be integrated on static developable surfaces[4,28,29], but cannot conform to dynamic non-developable biological surfaces. Moreover, these flexible phased arrays have limited spatial resolution, beamforming control and penetration depth. Therefore, stretchable electronics for non-invasive and continuous monitoring of deep tissues in the human body is still a grand challenge (Supplementary Discussions 1 and 2).

Here, we report a stretchable ultrasonic phased array that addresses this critical need (Fig. 1b). The elastic mechanical properties of the device allow for intimate and natural integration with the dynamic non-developable human skin for continuous and

[1]Department of Nanoengineering, University of California, San Diego, La Jolla, CA, USA. [2]Materials Science and Engineering Program, University of California, San Diego, La Jolla, CA, USA. [3]School of Electrical and Electronic Engineering, Yonsei University, Seoul, Republic of Korea. [4]Department of Bio and Brain Engineering, Korea Institute of Science and Technology, Seoul, Republic of Korea. [5]Department of Bioengineering, University of California, San Diego, La Jolla, CA, USA. [6]Department of Robotics Engineering, Daegu Gyeongbuk Institute of Science and Technology, Daegu, Republic of Korea. [7]Department of Anesthesiology and Critical Care, University of California, San Diego, La Jolla, CA, USA. [8]Department of Electrical and Computer Engineering, University of California, San Diego, La Jolla, CA, USA. [9]Present address: John A. Paulson School of Engineering and Applied Sciences, Harvard University, Cambridge, MA, USA. [10]These authors contributed equally: Chonghe Wang, Baiyan Qi, Muyang Lin, Zhuorui Zhang. ✉e-mail: shengxu@ucsd.edu

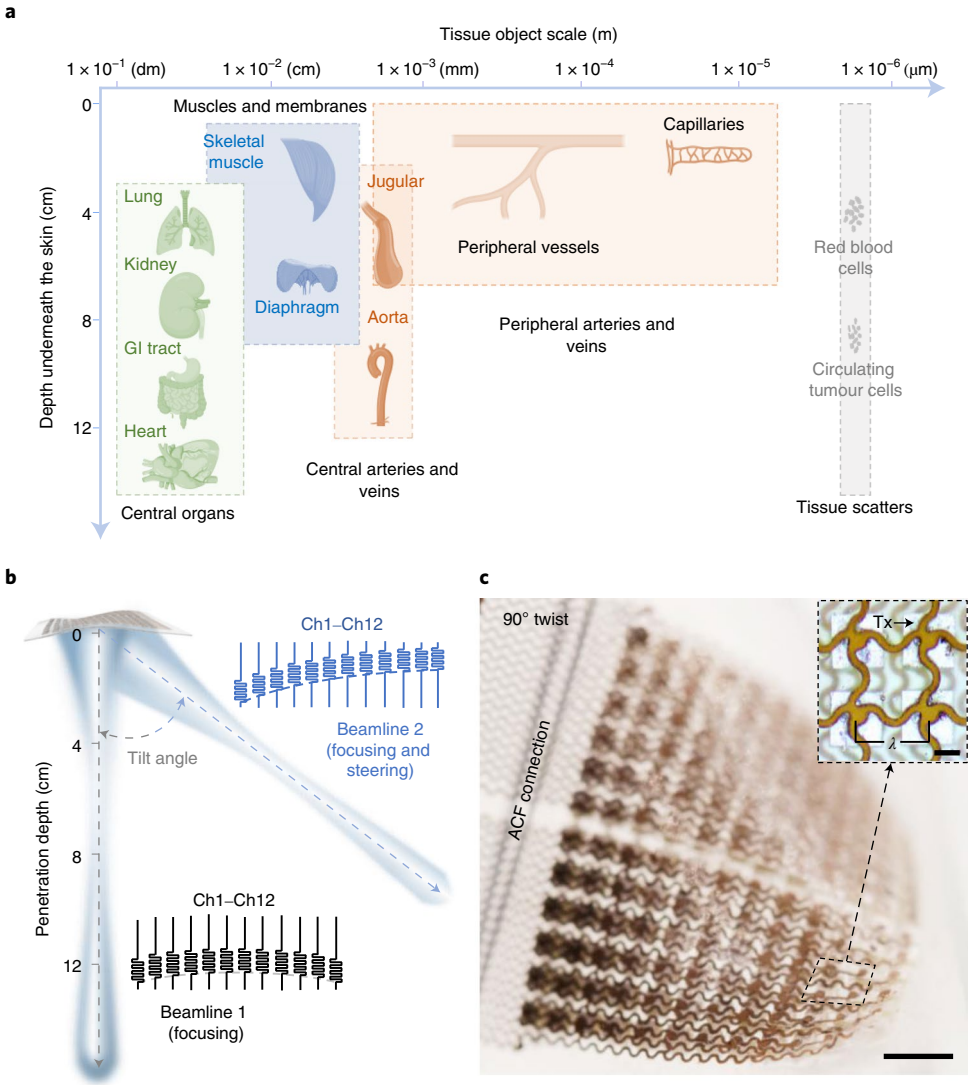

Fig. 1 | Challenges of deep-tissue monitoring and mechanism of the stretchable ultrasonic phased array. a, Depths underneath the skin (*y* axis) and dimensions (*x* axis) of representative human tissues and organs of interest. The stretchable sensor needs to have long penetration depths and to resolve structures at multiple scales. GI, gastrointestinal. **b**, Working principle of ultrasonic phased-array transmit beamforming. With a pre-designed pulse time profile, the phased array can focus and steer the ultrasonic beam to target regions of interest. Beamline 1 illustrates the penetration depth of a focused ultrasonic beam (up to 14 cm in human tissues). Beamline 2 illustrates the focusing and steering of the ultrasonic beam by adjusting the pulse time profile of the phased array. Ch, channel. **c**, Optical image of a 12 × 12 stretchable phased array twisted 90°, with bending and stretching of the interconnects. Inset: magnified image of four transducer (Tx) elements in the array, with an island bridge design and a pitch (λ) of 0.8 mm—approximately one ultrasonic wavelength at 2 MHz according to Huygens' principle. ACF, anisotropic conductive film. Scale bars, 2 mm (main image) and 300 μm (inset). Organ icons in **a** created with BioRender.com.

long-term monitoring. The seamless integration removes air gaps at the device–skin interface, which eliminates the requirement for ultrasound gels typically used for rigid and flexible ultrasonic devices[30]. We applied the phased-array control to every element for transmit and receive beamforming[31,32] (Fig. 1c). The resulting focused ultrasonic beam was much higher in intensity than that of an unfocused single element[17,18], which greatly enhanced the signal-to-noise ratio (SNR) of the reflection signals from deep tissues of dimensions from decimetres to micrometres. The relatively long wavelength of the ultrasonic waves largely enhanced the tolerance of beamforming to the phase aberration induced by the shape change of the device on the human skin. We could control the focal length and steer the direction of the ultrasonic beam from −20° to 20° (Fig. 1b), allowing for active targeting of specific regions of interest in the human body. As a proof of concept, we demonstrated the detection of left and right human heart ventricular Doppler signals ~3–14 cm beneath the skin. The ultrasonic beam could be steered to intercept blood flow at an appropriate Doppler angle, allowing accurate recordings of blood flow spectra in major arteries and veins[33]. Combining the blood flow and vessel dimension measurements, we were able to estimate cerebral blood flow in real time.

Based on Huygens' principle, the ultrasonic wavelength needs to be about the same as the pitch of the phased array to enable high-quality beam convergence[34]. The requirements on penetration depth and resolution place competing needs for the ultrasonic wavelength: a shorter wavelength has a better resolution but a lower penetration depth, and vice versa. We chose a wavelength of 770 μm (corresponding to a centre frequency of ~2 MHz) to reduce

the linear attenuation while maintaining sufficient resolutions[35]. This wavelength provides sufficient penetration for sensing tissues ~14 cm beneath the skin, with sufficient axial and lateral resolutions to differentiate major anatomic structures and fluid dynamics in major vessels[36]. The pitch of the device was therefore designed to be ~770 μm. Additionally, the 770-μm wavelength reduces the sensitivity of individual elements to the phase aberration caused by shape changes of the phased array when integrated on the human body. Each element in the phased array is connected with a serpentine wire to achieve individual element control and system-level stretchability. With a total thickness of 650 μm, the device has a low form factor and can be twisted or stretched. The device can easily conform to non-developable surfaces (Supplementary Figs. 1 and 2) and can be stretched elastically to an equal biaxial strain level of 16%, beyond which the interconnects undergo plastic deformations (Supplementary Fig. 3 and Methods).

The elements show comparable electromechanical coupling to commercial rigid probes, as well as highly consistent centre frequencies and electromechanical coupling coefficients across the entire array (Fig. 2a, Supplementary Fig. 4 and Supplementary Discussion 3)[37]. A single element has a spreading ultrasonic field, which will interfere with that of the adjacent element to create a converged beam at the focal point (Fig. 2b). A lower element frequency leads to a larger insonation area and better convergence (Supplementary Figs. 5 and 6). At the focal point, the beam intensity of a 1 × 12 linear array is much higher than that of the beam from a single element (Supplementary Fig. 7), resulting in substantial penetration of 14 cm in tissues. The phased array delivers 0.47 W cm^{-2} ultrasonic energy to deep tissues, which is within the safe range defined by the Food and Drug Administration (up to 190 W cm^{-2}; Supplementary Discussion 4)[38].

Tuning the pulse time profile of the phased array allows steering of the beam direction of a tilting angle from −20° to 20° in three-dimensional (3D) space (Supplementary Fig. 8, Supplementary Video 1 and Methods). 3D mapping of the ultrasonic beam shows the high penetration depth and excellent beam convergence of the device (Fig. 2c). A long focal length can narrow the beam width and improve the beam directivity, leading to better spatial resolution (Supplementary Fig. 9). The stretchable phased array has a similar beam directivity (in a wide range of tilting angles) to that of a commercial rigid phased array (Supplementary Fig. 10). The axial resolution of the stretchable ultrasonic phased array is much higher than that of electromagnetic devices[4] (Supplementary Discussion 5). The lateral resolution can be further increased with more elements in the linear array, such as from 12 in this study to 128 in commercial devices.

To further enhance the directivity and intensity of the beam, and therefore the lateral resolution and SNR, we excited elements in multiple rows (Supplementary Figs. 8 and 11) and multiple pulses together (Supplementary Figs. 12 and 13). The associated benefits were threefold. First, multi-row excitation generates a more focused ultrasonic beam, which gives a better lateral resolution and produces a higher SNR, which is critical for sensing small reflectors (for example, red blood cells). For imaging applications, the SNR should be above 18 dB[39,40]. In vitro characterization of the SNR along the main beam demonstrated an SNR of >18 dB, even at 20 cm depth for all incident angles (Fig. 2d and Methods). Second, multi-pulse excitation has a much smaller bandwidth. For example, 15 pulses have a bandwidth of 5.72%, compared with 24.58% for a single pulse (Supplementary Fig. 12). A smaller bandwidth leads to a higher sensitivity to the Doppler shift, which is beneficial for sensing small reflectors (Supplementary Discussion 6)[41]. Third, multi-pulse excitation enhances the tolerance of beamforming to shape changes of the stretchable phased array. In this study, activation of a minimum of three rows (a 3 × 12 array) was required to generate sufficient signal strength for sensing haemodynamics in deep tissues. This activation scheme consumes 36 times the power of a single element. The power budget of three rows (0.25 W) is still manageable for wearable devices (Methods).

To date, phased-array beamforming has only been implemented in rigid[24–26] and flexible[27–29] probes, because correcting the phase aberration induced by changes in the pitch of a stretchable phased array remains a grand challenge. When a stretchable device undergoes tensile or compressive strain, each element is displaced from its predefined location, causing deviations in the acoustic interference and thus beamforming. Although auto-correction methods can measure the location of each element and minimize the associated phase aberration[42], the dynamic curvilinear human skin poses a daunting task for tracking elements' locations accurately in real time. In this work, we chose a relatively long wavelength of 770 μm, which has sufficient axial resolution and reflection intensity from small reflectors (Supplementary Discussion 7)[43]. Most importantly, this relatively long wavelength minimizes the sensitivity of beamforming to shape changes of the device in any direction. Moreover, the multi-pulse excitation enables a higher probability of interference; therefore, beamforming is enhanced (Supplementary Fig. 13), which further minimizes the sensitivity of beamforming to device deformation.

To quantify how the long wavelength mitigates the phase aberration, we first investigated the phase error created by the dynamic curvature of the human skin. With a 3D scanner, we measured the minimum curvature radius of a human neck in different postures to be ~4.2 cm (Supplementary Figs. 14 and 15). Figure 2e shows the required pulse time profile for a linear array on a flat surface (blue bars) and deviation on a surface with a curvature radius of ~4.2 cm (orange bars) to create a synthetic wave front at the same focal point. The deviation is the largest for the element on the edge of the array (corresponding to a phase aberration of 4.26%) and is the smallest for the element at the centre (corresponding to a phase aberration of 0.06%). Therefore, at an ultrasonic wavelength of 770 μm, the phase aberration from typical neck skin is relatively small and has

Fig. 2 | Performance characterizations of the stretchable ultrasonic phased array. a, Impedance and phase-angle spectra of a single piezoelectric transducer after integration into the stretchable array, showing a centre frequency of 1.96 MHz, an antiresonance frequency of 2.06 MHz, a phase angle of 75° and an electromechanical coupling factor k_t of 0.61. **b**, Mapped ultrasonic field of a single element transducer (Tx, 2 MHz, 0.55 mm × 0.55 mm × 0.6 mm (length × width × thickness)). The inset is the cross-section of the insonation region in the *x*–*y* plane, with the position and size of the element marked by the square, to show the beam spreading of a single element. Scale bars, 5 mm (main image) and 3 mm (inset). **c**, Mapped ultrasonic field of the phased array in three dimensions. The scale bars in all directions are 1 cm. Inset: magnified cross-section of the ultrasonic field at the focal point, demonstrating good beam convergence in the *x*–*y* plane. Scale bar, 1 cm. **d**, Characterization of the SNR along the beam in water, showing a high SNR at different incident angles. The blue shaded region indicates that an SNR above 18 dB is typically needed for high-quality imaging. **e**, Top: effect of the shift in elements' positions on the phased-array beamforming performance. The blue bars denote the required time delay of the pulse signal sent to each element on a planar surface. The orange bars denote the required correction to achieve the same beamforming outcome on a curved surface with a curvature radius of 4.2 cm (that is, the minimum radius of the human neck in normal postures in this study). Bottom: schematic image showing the propagation and convergence of the synthetic wavefronts of the phased array. **f**, Mapped ultrasonic fields demonstrating beam steering from −20° to 20° on a curved surface with a curvature radius of 4.2 cm. The results show a high-intensity main beam and a low-intensity grating lobe when the incident angle is large. Scale bars, 0.5 cm. Panels **c** and **f** share the same intensity bar.

minimal effect on the phased-array beamforming (Supplementary Discussions 7–9). For theoretical modelling of wave propagation, see Supplementary Video 2.

Then, to test the beamforming of the stretchable ultrasonic phased array on a complex surface, the device was laminated on a tissue-mimicking phantom replicated from the human neck. Testing results showed that on both planar and phantom surfaces the ultrasonic beam could be steered in a wide range of incident angles (Extended Data Fig. 2 and Supplementary Fig. 16). The working range for high-accuracy sensing is defined as the range in which the intensity of the grating lobe is at least −15 dB weaker than the main beam[44]. When the device follows the contours of the phantom, the working range is from −20° to 20° (Fig. 2f), with a 0.1° accuracy of the post-end testing system (Methods). The beam tilting of this phased array enables active targeting of regions of interest over a wide range, which is impossible for single transducers or annular arrays that can only adjust focal depth directly below the transducers[45]. Besides bending, the performance of the phased array was

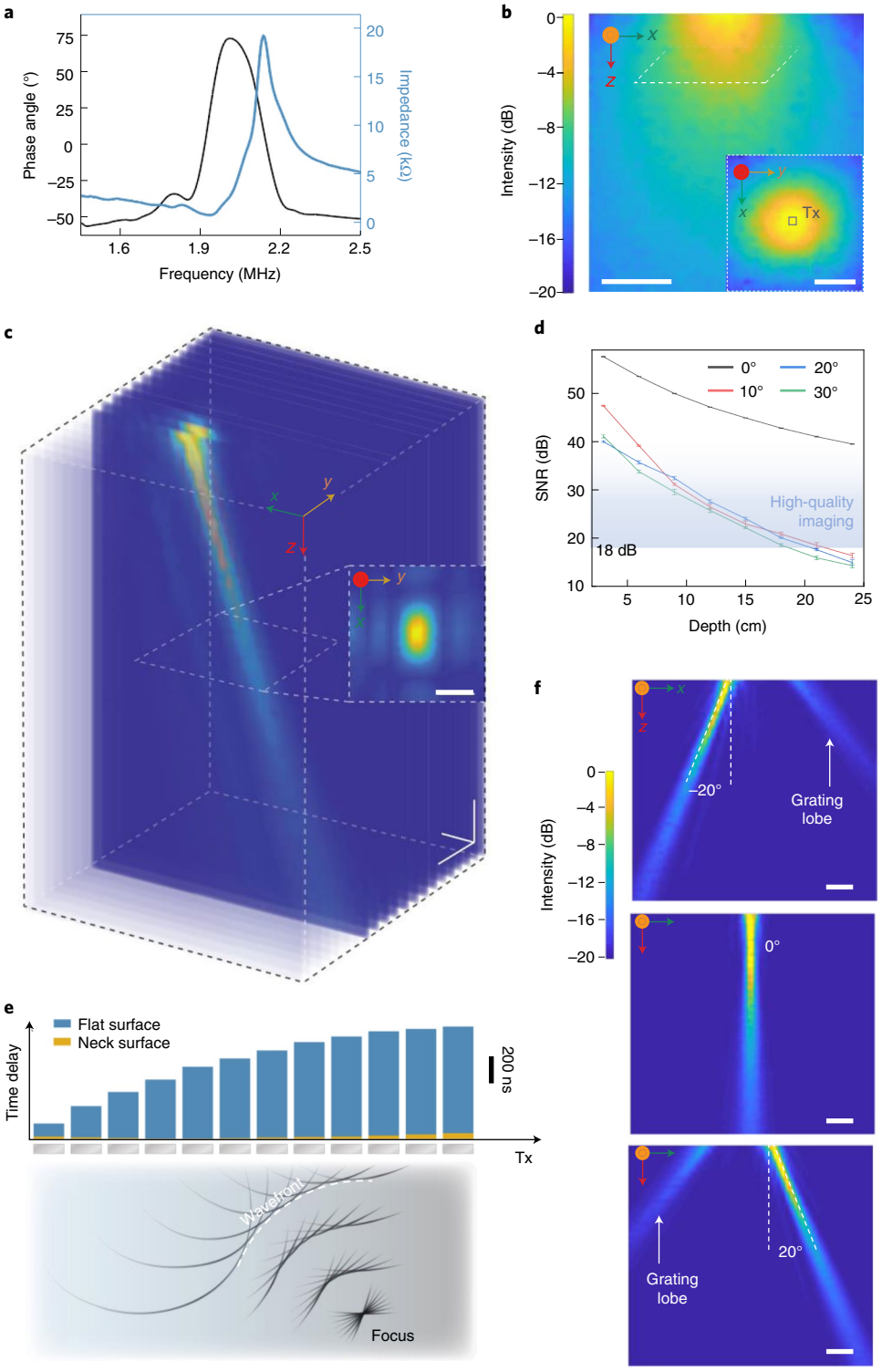

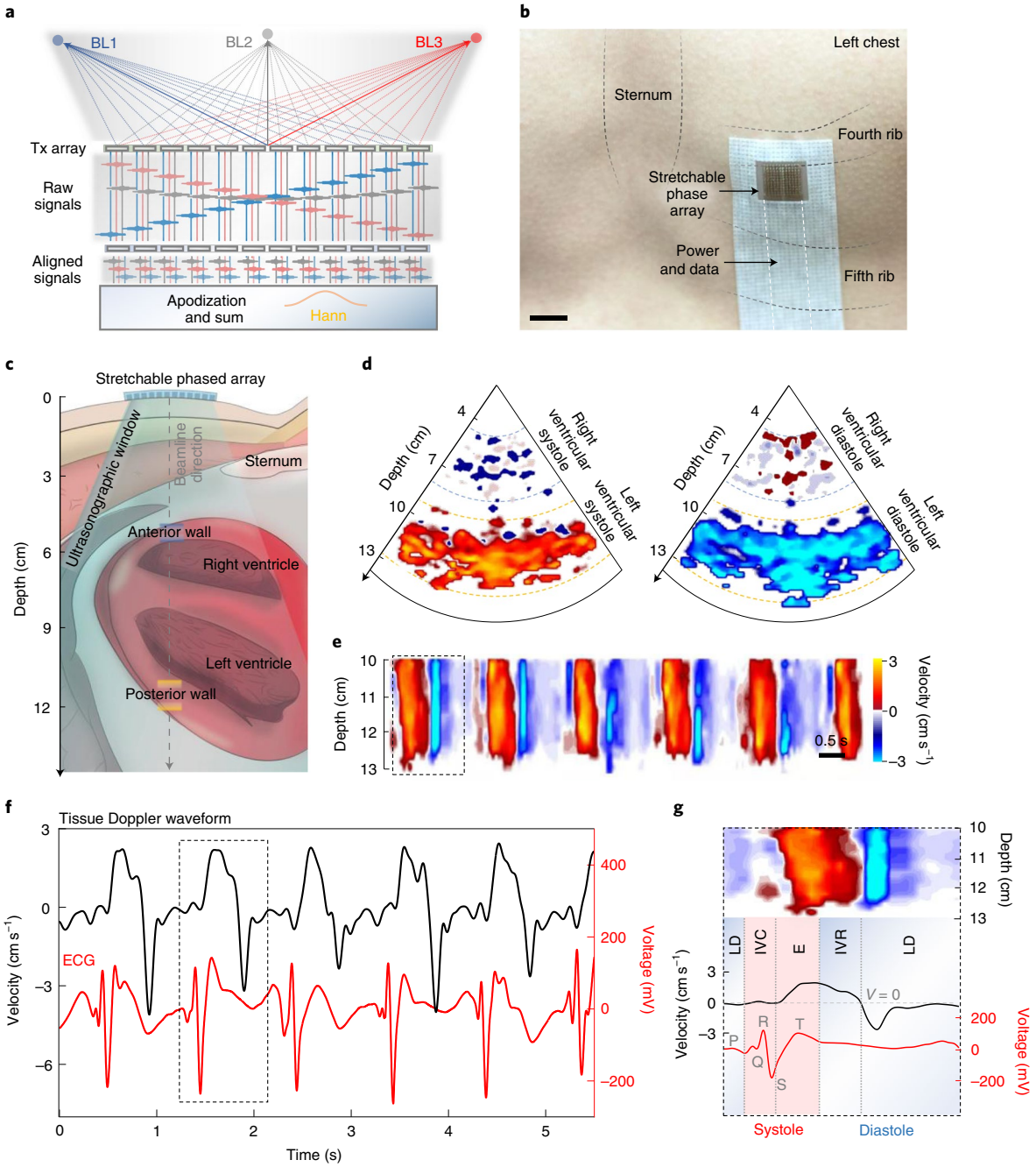

Fig. 3 | Cardiac activity monitoring. a, Working principle of phased-array receive beamforming. The SNR of the signal can be enhanced by delaying and summing the raw signals received by each transducer channel. The signal can be a weighted sum with the choice of proper window functions (for example, the Hanning function) to further enhance the contrast. BL, beamline; Hann, Hanning window function. **b**, Optical image of the device on the human chest. The key components are labelled. Scale bar, 1 cm. **c**, Schematic of the ultrasonographic window used in cardiac activity monitoring. The 0° beamline, anterior wall of the right ventricle (blue) and posterior wall of the left ventricle (orange) are labelled. **d**, Doppler spectra of the ventricles, clearly showing systole (left) and diastole (right) of both the right ventricle and left ventricle. Orange/red indicate tissue movement towards the device, whereas blue indicates movement away from the device. Brighter colours indicate faster tissue movements. **e**, Detailed Doppler spectra analysis of the left ventricle posterior wall, clearly demonstrating systolic and diastolic phases during cardiac cycles. **f**, Tissue Doppler waveform of the left ventricular posterior wall (black curve; showing the systolic and diastolic velocities) and ECG waveform (red curve) measured simultaneously. **g**, Magnified image of simultaneously measured tissue Doppler spectra from the dashed box in **e**, along with the tissue Doppler waveform and ECG signal from the dashed box in **f**, showing the correspondence of the three signals in one cardiac cycle, including systole (red; iso-volumetric contraction (IVC) and ejection (E)) and diastole (blue; iso-volumetric relaxation (IVR) and late diastole (LD)). Panels **d**, **e** and **g** share the same velocity bar.

also characterized under in-plane deformations. The results showed that the beamforming is reliable under 20% tensile or compressive strain, which is typically the maximum strain of the human skin in a natural posture (Supplementary Fig. 17).

With strong penetration and well-controlled beam focusing and steering characteristics, even on curvilinear surfaces, the stretchable ultrasonic phased array has broad implications for targeted deep-tissue monitoring. We focused this technology on cardiovascular

systems that dominate mortality in organ failure[1] and demonstrated two applications: in cardiac tissue Doppler imaging at a depth of ~3–14 cm beneath the skin; and in blood flow spectrum recording (with red blood cells several micrometres in size) for quantitative analysis of central cardiovascular dynamics.

Echocardiography is widely used for non-invasive direct diagnoses of cardiovascular diseases, such as cardiomyopathy[46] and valvular diseases[47–50], but is mostly conducted in clinics only, with data captured only at the point of care[51]. Typical echocardiographic probes are rigid and bulky, making them impractical for chronic patient monitoring. Moreover, obtaining high-quality data from these probes in current clinical settings requires extensive labour and high cost[52]. Longitudinal echocardiographic measurements of cardiac functions have therefore not been available. Monitoring of cardiac functions relies on either invasive probes (for example, pulmonary artery catheter) or non-invasive probes that provide indirect estimates based on relevant parameters (for example, arterial waveform analysis, impedance changes and aortic Doppler). The stretchable ultrasonic phased array, which may be considered as an ultrasound-based Holter monitor, allows direct probing of cardiac sites and interrogation of myocardial dynamics, and thus holds promise for ambulatory management of cardiac functions.

Since ventricular structures are ~3–14 cm beneath the human skin, ventricular signals experience huge attenuation in both the transmitting and receiving processes[53]. The quality of the received signals depends not only on the transmitting beam intensity, but also the receiving performance of the phased array. To enhance the SNR of the received signals, we utilized receive beamforming (Fig. 3a)—a reverse process of the transmit beamforming[31]. The receive beamforming takes into account the signals received by all elements in the array, compensates for their phase differences and then adds up the signals to reconstruct a stronger echo with a higher SNR (Supplementary Fig. 18). With transmit and receive beamforming, the stretchable phased array can detect objects in various orientations up to 17 cm deep in water (Supplementary Fig. 18), as well as tissue-mimicking phantoms (Supplementary Fig. 19 and Supplementary Video 3). The results were validated in the same condition with a commercial device (Supplementary Fig. 19).

Figure 3b,c illustrates the operational setup of the stretchable ultrasonic phased array and schematic cardiac anatomy when the device is placed between the fourth and fifth ribs (Supplementary Fig. 20 and Methods). By decoding the Doppler shift in the entire ultrasonographic window, tissue Doppler images can be reconstructed to show the ventricular wall motions in real time. Figure 3d shows the simultaneous contractions of the right and the left ventricular walls in the systole phase (left) and their relaxation in the diastole phase (right). A close-up of the velocity profile at a depth of ~10–13 cm reveals the periodic systolic and diastolic pattern of the left ventricular posterior wall (Fig. 3e and Extended Data Fig. 3). Figure 3f shows the correlation between the tissue Doppler waveform (black curve) and electrocardiogram (ECG) (red curve; Supplementary Fig. 21 and Methods). Figure 3g shows the tissue Doppler spectrum, waveform and ECG recorded simultaneously. The two phases of systole can be clearly identified. In the iso-volumetric contraction (IVC) phase, the atrioventricular valves close. This IVC phase is then followed by the ejection period, during which the aortic valve opens, blood is discharged into the aorta, and the ventricular ejection reaches its highest velocity. Diastole consists of two phases. The early iso-volumetric relaxation phase is represented by a decrease in the ventricular velocity curve to zero, when all valves are closed. Following this is the late-diastole phase, during which the atrioventricular valves open, allowing the ventricles to begin to refill. The cardiac phases acquired by the stretchable ultrasonic phased array match well with the cardiac cycle traced by the ECG. The measured tissue Doppler provides a direct quantitative assessment of specific myocardium, which complements conventional ECG and stethoscope measurements[49]. The continuous direct insights on anatomies and functions of cardiac tissues offered by the stretchable ultrasonic phased array may be valuable for acute disease prognosis and post-surgery monitoring[54].

Continuous blood flow monitoring can be useful for long-term evaluation of tissues or organs at risks, such as blood supply to the cerebrum or the lower extremities in patients with vascular diseases[11,55–57]. At present, there are several skin- or tissue-integrated devices that show promise for accurate long-term blood flow monitoring[11,58]. However, these devices cannot quantitatively assess the blood flow rate, which is the key to analysing tissue blood supply[59]. Doppler ultrasonography is widely considered as the gold standard for quantitative blood flow measurements in central blood vessels, but similar to echocardiography, Doppler ultrasonography is generally limited to point-of-care applications. The stretchable ultrasonic phased array allows monitoring of blood flow in major arteries and veins quantitatively and continuously.

In this study, we focused on measuring the blood flow in the carotid artery and the neighbouring jugular vein because they are the key pathways for cerebral blood supply and drainage[60]. Compared with specular reflection signals (for example, those from cardiac muscle interfaces), signals from red blood cell scattering have a much lower intensity due to the much smaller size of the scatters (~8 μm in diameter) than the ultrasonic wavelength

Fig. 4 | Central blood flow monitoring. a, Working principle of ultrasonic Doppler sensing. The device sends a focused beam at an incident angle of ~20° to moving red blood cells. Inset: interaction between an ultrasonic pulse and a moving red blood cell. **b**, Optical image of the device on the human neck. The key components are labelled. **c**, Colour flow image reconstructed from reflection signals received by the device. The beam direction is marked by the dashed orange line. The reflection signal intensity is in the grey scale. The insonation area achieved with the stretchable phased array is comparable to a commercially available device (Supplementary Fig. 19). The initial resonance area (whitened area) immediately beneath the device is due to the transducer's ringing effect[71]. The colour flow image clearly shows the jugular venous (blue) and carotid arterial (red) flows with depth and directional information. The magnitude of the flow velocity is in the colour scale, with red flowing towards the device and blue flowing away from it. Fw, forwards; Bw, backwards. **d**,**e**, Colour flow images of the carotid artery (**d**) and jugular vein (**e**). The Doppler angles in **d** and **e** are 58° and 54°, respectively. **f**,**g**, Carotid artery (**f**) and jugular vein (**g**) flow spectra, compared with those of a commercial rigid ultrasonic device. EDV, end-diastolic velocity; PSV, peak systolic velocity. **h**, Bland–Altman analysis of the PSV of carotid arterial flow measured by the stretchable phased array. The stretchable phased array yields a biased error (μ) of 0.046 m s^{-1} and a precision error (σ) of 0.191 m s^{-1}, comparable to the commercial device ($\mu = -0.035$ m s^{-1}; $\sigma = 0.175$ m s^{-1}). **i**, Bland–Altman analysis of the EDV of the carotid arterial flow measured by the stretchable phased array. The stretchable phased array yields $\mu = 0.004$ m s^{-1} and $\sigma = 0.047$ m s^{-1}, comparable to the commercial device ($\mu = -0.002$ m s^{-1}; $\sigma = 0.040$ m s^{-1}). In **h** and **i**, the solid horizontal lines represent the mean difference and the dashed lines represent ±1.96 standard deviations. **j**, Cerebral blood circulation volume calculated by measuring the CBF over a period of 30 min on three participants. Note the spike at minute 15, indicating an exercise-induced increase in CBF. Centre values for minutes 0, 5, 10, 15, 20, 25 and 30, respectively, are 0.71, 0.81, 0.62, 1.56, 0.83, 0.45 and 0.60 l min^{-1} for the stretchable phased array and 0.48, 0.78, 0.6, 1.58, 0.74, 0.45 and 0.80 l min^{-1} for the comparator. Measures of dispersion (σ) for minutes 0, 5, 10, 15, 20, 25 and 30, respectively, are 0.23, 0.11, 0.11, 0.12, 0.16, 0.16 and 0.12 l min^{-1} for the stretchable phased array and 0.04, 0.03, 0.13, 0.11, 0.17, 0.13 and 0.12 l min^{-1} for the comparator. Error bars represent standard deviation of the CBF. Replicates were biological. Scale bars, 1 cm (**b**) and 5 mm (**c**–**e**).

(Supplementary Fig. 22). Phased-array transmit and receive beamforming creates a high SNR, which enables sufficient ultrasonic energy scattered from groups of red blood cells (note that it is not from a single red blood cell) to compute blood flow signals (Supplementary Fig. 23). By extracting the Doppler shift and vessel orientation (Supplementary Figs. 24 and 25), the blood flow velocity can be calculated by equation (1)[33]:

$$V = \frac{c f_d}{2 f_0 \cos\theta} \quad (1)$$

where V is the flow velocity, c is the ultrasonic wave speed in human tissues (~1,540 m s^{-1}), f_d is the captured Doppler shift, f_0 is the centre frequency of the transducer and θ is the Doppler angle between the beam and the blood vessel.

The stretchable phased array is placed on the human neck and the ultrasonic beam is focused and steered to achieve optimal insonation of the carotid artery and jugular vein (Fig. 4a,b). The amplitude and Doppler frequency shift of the received signals can be used to reconstruct a colour flow image (Fig. 4c), which depicts tissue structures in a grey scale and blood flow in a colour scale[61]. To accurately record the flow velocity, the Doppler angle should not exceed 60°, beyond which errors are induced[33] (Fig. 4d,e, Supplementary Figs. 25 and 26 and Methods). The measured flow spectra of the carotid artery and jugular vein show characteristic cardiac pulsation patterns (Fig. 4f,g). The peak systolic and

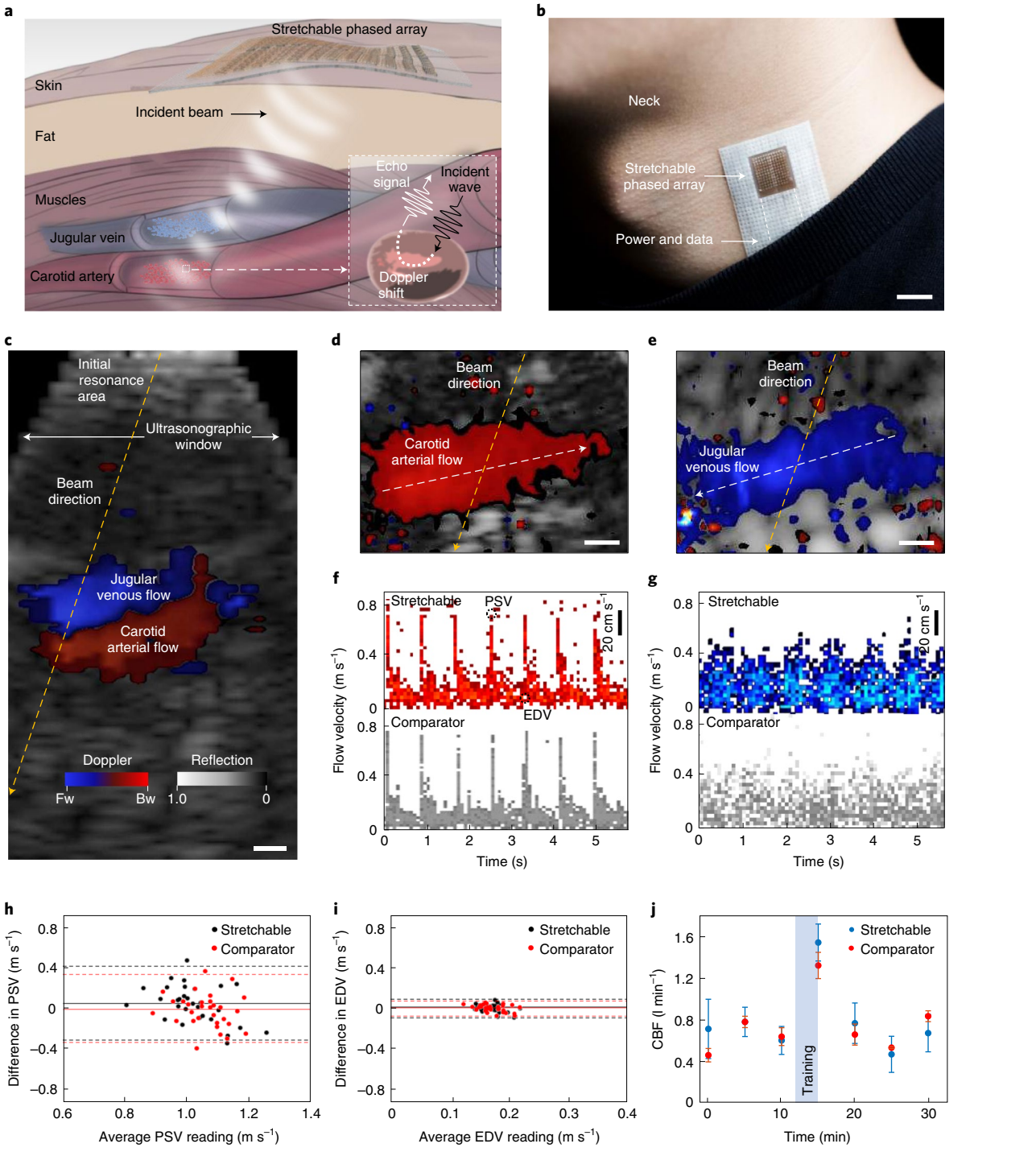

end-diastolic velocities, which are of particular interest for haemodynamic analysis, can be identified directly on the spectra. To validate the results, the stretchable phased array (top curves in Fig. 4f,g) and a commercial phased array (bottom curves in Fig. 4f,g) are used to measure the flow velocity simultaneously (Methods). The measurements were repeated 30 times on three healthy participants with both devices. Bland–Altman analysis of the data shows a high level of agreement, demonstrating that the precision and accuracy of the stretchable device, without any calibration, are comparable to those of the commercial one (Fig. 4h,i)[62]. The stretchable phased array can be readily integrated with the skin, eliminating the need for manual holding and scanning (Supplementary Fig. 27), which enables stable recordings of central blood flow for at least 7 d, with 1 h of continuous recording per day (Supplementary Figs. 28 and 29). The stretchable device is robust with minimal performance degradation after 60 d of repetitive use (Supplementary Fig. 30).

Cerebral blood circulation is critical for sustaining the central nervous system, and it is easily affected by changes in acceleration and microgravity, as well as vascular diseases[63]. So far, it has been difficult to evaluate cerebral circulation using non-invasive methods. Stretchable electronics that can record blood flow volume continuously over the long term meet this critical need[64,65]. Because carotid arteries are the key pathway to the brain, the carotid blood flow (CBF) can be correlated with the volume of cerebral blood circulation[66]. CBF can be measured using a handheld rigid ultrasonic probe. However, this method is limited to diagnosis in the hospital and requires steep operator training, and the results can be highly operator dependent[67].

With the stretchable ultrasonic phased array, the flow velocity inside a blood vessel and the vessel diameter can be measured simultaneously (Supplementary Fig. 31). Multiplying the average CBF velocity by the vessel cross-sectional area yields the CBF (Supplementary Discussion 10). We measured the CBF of a participant over a period of 30 min with 5-min intervals, with the participant resting during the first 12 min then performing a 3-min burpee test during minutes 13–15 (Fig. 4j, shaded in blue) and resting in the last 15 min[68]. From the data, it was clear that at minute 15 the CBF increased from 0.590–1.560 l min^{-1}. After the participant rested for 5 min, the CBF returned to the baseline (Fig. 4j). The results showed good reproducibility, as evidenced by the error bars from three consecutive measurements on the same participant, with a measurement precision of 0.421 l min^{-1} ($n=3$). The CBF measurement results were validated against those from a commercial device (Fig. 4j). During the entire process, seamless integration of the stretchable device to the skin removed the need for ultrasound gel, yielding negligible degradation in signal quality, even with hairs on the skin (Supplementary Figs. 32–34).

The stretchable ultrasonic phased array reported here opens up a new sensing dimension for existing stretchable electronics. The sensing range of the stretchable phased array is no longer limited to areas directly below the device, but expands to a much wider window. The capability of steering the ultrasonic beam enables active targeting of deep tissues of interest. Leveraging the phased-array transmit and receive beamforming, the device has a high SNR and maintains a high resolution for sensing groups of microscale objects, such as red blood cells. The accessible deep tissues are not limited to those studied in this work but can be extended to many others, providing critical capabilities for perfusion monitoring and continuous surveillance of organs at risk for many patients. Technical challenges still remain before we deploy this preliminary prototype to other general settings. For example, the front-end sensor still requires wired data outputs to the back-end acquisition system for post-processing (Supplementary Fig. 35). Ongoing research efforts are focusing on integrating the sensors with on-board signal pre-conditioning, memory and wireless data transmitting, and replacing the power supply with a state-of-the-art flexible lithium-polymer battery. Additionally, the combined strategies of low-frequency and multi-pulse excitation in this work bypass the requirement of calculating the relative position and phase of each element in the phased array. For future applications that require an enhanced spatial resolution, we will develop adaptive algorithms following the time reversal principle, which uses reference points in the tissue to correct the phase aberration of each element induced by the skin deformation.

Methods

Human testing protocols, specifications and anatomical data. The commercial probe used to validate the stretchable phased array was a Verasonics P4-2v phased-array transducer. The P4-2v probe contains 64 elements with a pitch of 0.3 mm, an elevation focus of 50–70 mm and a sensitivity of around −69 to −95 dB. All measurements were conducted following a standard ultrasound probe operational procedure. The blood flow was measured on three healthy participants in a static sitting position. All human tests were approved under University of California, San Diego Institutional Review Board (IRB) protocol 170812. All participants gave voluntary consent to blood flow measurements and skin curvature characterizations. The anatomical data that appear in Figs. 1 and 3, Extended Data Fig. 3 and Supplementary Fig. 20, including the dimensions and locations of central organs and deep tissues, are from the Complete Anatomy platform (copyright 2019; 3D4Medical, Elsevier; https://3d4medical.com/). Using this software, we measured the depth of each listed organ, including the heart, lung, gastrointestinal tract, vascular system and so on. The model used in Complete Anatomy is a representation of a typical human participant; thus, we acknowledge that there may be variations between the model and specific participants with regard to age, gender, ethnicity and body conditions[69].

Biaxial mechanical testing and strain measurement protocols. During tensile testing, we measured the strain by tracking the distance variation between two adjacent elements on a customized stretcher. The tensile experiments were performed under an optical microscope coupled with a charge-coupled device camera and an imaging software system (10× magnification). We were able to continuously and accurately track and measure the centre-to-centre distance of two adjacent elements both laterally and horizontally.

Scalability of the array size, device layout designs, resolution testing, activation scheme, directivity analysis, intensity comparison, power consumption and simulation conditions. The array number was not limited to 12 × 12 in this work. By adopting the fabrication technique of a multi-layered stretchable circuit[70], the array number could be scaled up without physical constraints. The mass production of the stretchable design could be accomplished by standard microfabrication with high yield and low cost. Compared with the unfocused ultrasonic device developed previously[17,18], we decreased the centre frequency of the elements from 7.5 to 2 MHz and reduced the element pitch from 2.5 mm × 2 mm to 0.8 mm × 0.8 mm. Therefore, the element density was increased by 7.8-fold to achieve a higher energy density for deep-tissue penetration. For phased arrays, systems typically employ a $\lambda/2$ pitch to avoid grating lobes. We did not use the $\lambda/2$ pitch here because this $\lambda/2$ pitch would require dicing of the piezoelectric 1–3 composite materials to ~0.3–0.4 mm in size with 1 mm thickness, which was very challenging with the existing facilities. Also, the small pitch would largely reduce the stretchability of the entire device.

The resolution was characterized by applying the line spread function[17]. B mode images were taken in water using the stretchable ultrasonic phased array (with a 4-cm focal length). All radiofrequency data were sampled and processed using the Verasonics system. The beamline tilt resolution was 0.1°, controlled by the Verasonics system. An iron wire with a diameter of 0.5 mm was placed at depths of 5, 10, 20 and 30 cm beneath the device. By calculating the imaged diameter of the iron wire, the axial resolution could be calculated. We activated three rows (36 elements) simultaneously to generate sufficient signal strength to accomplish the applications in this work. The power consumption of the device under this excitation scheme was 0.25 W (25 V, 5,000 Hz and ten pulse excitations). This power budget could potentially be met by a commercial lithium-polymer battery. We observed very minimal heating while using an activating voltage of 25 V (Supplementary Figs. 36–38). The surface temperature of the device barely rose. These results showed the feasibility of integrating the stretchable phased array in a fully wearable system for future low-power, long-term central haemodynamic recording.

The axial resolutions of the stretchable phased array are listed in Supplementary Discussion 5. The directivity, penetration and intensity calculations of the device, as shown in Supplementary Figs. 5–7, 10 and 12, were performed in Field II, MATLAB (MathWorks). Except for the centre frequency and transducer geometry, all conditions were set to be identical, including the input excitation voltage, single-cycle pulse and electromechanical coupling coefficient. The attenuation coefficient of the media was defined as 0.75 dB cm^{-1} MHz^{-1} to mimic human tissues.

System setup, beam steering and optimal insonation adjustment. The stretchable phased array contains two parts, including the front-end probe and the back-end electronics and customized software (Supplementary Fig. 35). The front-end is a stretchable patch, which can be attached to the area of interest on the skin. To

connect all channels to the post-end Verasonics system, we designed a flexible and stretchable elongating region. This elongating region was for strain isolation between the stretchable front-end patch and the rigid adaptor and the post-end system (Supplementary Fig. 35). The length of the elongating region was decided by the application needs in consideration of the distance between the post-end system and the human participant. The elongating region was bonded to an anisotropic conductive film, which was then connected to a customized circuit board. The circuit board contained an array of Bayonet Neill–Concelman connectors and cables, which could be connected to the Verasonics system for signal processing and analysis. The participant under test could freely move in a considerable range with the patch adhered to the skin surface. The back-end electronics and customized software were all contained in the Verasonics system (Vantage 64). The ultrasonic beam could be steered to any pre-designed angle instantly. After laminating the patch on the skin, we first adopted the mode of colour flow image to locate the tissue of interest, including the depth and orientational angle relative to the device centre. Then, we adjusted the optimal insonation, which used the relative positional information to steer the ultrasonic beam to the region of interest.

SNR measurements. The SNR data were measured using a 3D ultrasonic mapping system (AIMS III hydrophone scanning system; Onda Corporation). The key components of the system include an automated scanning tank, a motion controller, an oscilloscope and a computer with embedded imaging software. The automated scanning tank is composed of a 3D linear motor, a rotator and a hydrophone, which can achieve 3D spatial and angular mapping of ultrasonic fields (positioning repeatability: <5 μm; x, y, z step size = 5.5 μm).

The SNR of any given point in the ultrasonic field was measured and calculated via equation (2):

$$\mathrm{SNR} = 20\log[\frac{V_{\mathrm{beam}}}{V_{\mathrm{noise}}}] \quad (2)$$

where V_{beam} is the peak voltage at a specific spatial point of the ultrasonic beam measured by the hydrophone, and V_{noise} is the voltage amplitude of the noise in the A mode measured by the hydrophone.

ECG measurements. ECG was simultaneously recorded with the tissue Doppler imaging on the same participant using the SphygmoCor EM3 device (AtCor Medical) (Supplementary Fig. 21). The healthy participant was in a sitting position with an ECG electrode on each arm and a common ground electrode on the left leg above the ankle.

Maximum skin curvature and strain characterization of the human neck. The skin curvature of the human neck was characterized using a high-resolution 3D scanner (HDI Advance; LMI Technologies). The field of view (FOV)-dependent accuracy of the scanner is 40 μm at 200 mm FOV, 65 μm at 400 mm FOV and 85 μm at 600 mm FOV. The duration was 1.2 s per scan. Skin curvatures were measured on 20 participants of different age, gender and ethnicity (Supplementary Fig. 14). The 3D scanning and model reconstruction were carried out with the FlexScan3D software (Polyga). The skin strain was measured on three participants in four postures, including head rotation to the left and right (with yaw angles from −60° to 60°) and flexion/extension (with pitch angles from −37° to 30°).

Colour flow image, tissue Doppler processing, filtering and vessel angle recognition. The colour flow imaging was applied to cardiac tissue Doppler imaging and blood flow imaging. The spectrum was decoded and displayed instantly by Verasonics. For cardiac tissue Doppler imaging, since the left and right ventricles have a depth range of ~3–14 cm, we extracted the Doppler signal in the entire ultrasonographic window. The tissue Doppler waveform was extracted by averaging the speed of the spectrum signal from a tissue depth of 10–13 cm. For blood flow imaging, we adopted a range-gated method to selectively extract Doppler signals from the vessel lumen region, so that the Doppler signals from pulsating vessel walls were removed. The vessel angle was calculated from the colour flow image using an image-processing algorithm. A finite impulse response filter (13 taps; −60 dB at a pulse-repetitive frequency of <0.003 and −3 dB at a pulse-repetitive frequency of 0.08) was added to improve the image quality. All of the coloured pixels in the vessel lumen region were used to calculate the flow direction vector, and to estimate the vessel angle and, therefore, the Doppler angle for calculating the flow velocities.

CBF measurements. As shown in Supplementary Fig. 31, there was a 4 × 5 unfocused ultrasonic patch (7.5 MHz) laminated at the top and a phased-array patch (2 MHz) laminated at the bottom. The 7.5-MHz patch was used for carotid artery blood vessel diameter recording, whereas the 2-MHz patch was for blood flow recording. We used the 7.5-MHz patch for recording the vessel diameter, which needed a high spatial resolution for resolving tissue interfaces. We used the 2-MHz patch for recording the flow velocity, which had a sufficient SNR. The 7.5-MHz patch directly recorded the vessel diameter underneath. The 2-MHz patch focused and steered the beam with a certain incident angle towards the 7.5-MHz patch direction so that we could study the vessel diameter and blood flow velocity at the same location. In this way, we could monitor and correlate these two physiological signals simultaneously. The required tilting angle depended on the inclination angle of the carotid artery. Due to the large difference in centre frequencies (7.5 and 2 MHz), there was not any noticeable crosstalk that would affect the signal quality of either patch.

Reporting Summary. Further information on research design is available in the Nature Research Reporting Summary linked to this article.

Data availability

The main data supporting the results in this study are available within the paper and its Supplementary Information. Data generated in this study, including source data and the data used to produce the figures, are available from Harvard Dataverse at https://dataverse.harvard.edu/dataset.xhtml?persistentId=doi:10.7910/DVN/EPITIY.

Received: 24 July 2020; Accepted: 10 June 2021;
Published online: 16 July 2021

References

1. Tran, D. D., Groeneveld, A., Nauta, J., van Schijndel Strack, R. & Thijs, L. Age, chronic disease, sepsis, organ system failure, and mortality in a medical intensive care unit. *Crit. Care Med.* **18**, 474–479 (1990).
2. Knaus, W. A., Draper, E. A., Wagner, D. P. & Zimmerman, J. E.Prognosis in acute organ-system failure. *Ann. Surg.* **202**, 685–693 (1985).
3. Tsai, M.-H. et al. Organ system failure scoring system can predict hospital mortality in critically ill cirrhotic patients. *J. Clin. Gastroenterol.* **37**, 251–257 (2003).
4. Agrawal, D. R. et al. Conformal phased surfaces for wireless powering of bioelectronic microdevices. *Nat. Biomed. Eng.* **1**, 0043 (2017).
5. Gao, W. et al. Fully integrated wearable sensor arrays for multiplexed in situ perspiration analysis. *Nature* **529**, 509–514 (2016).
6. Someya, T., Bao, Z. & Malliaras, G. G. The rise of plastic bioelectronics. *Nature* **540**, 379–385 (2016).
7. Rogers, J. A., Someya, T. & Huang, Y. Materials and mechanics for stretchable electronics. *Science* **327**, 1603–1607 (2010).
8. Kim, J. et al. Battery-free, stretchable optoelectronic systems for wireless optical characterization of the skin. *Sci. Adv.* **2**, e1600418 (2016).
9. Chung, H. U. et al. Binodal, wireless epidermal electronic systems with in-sensor analytics for neonatal intensive care. *Science* **363**, eaau0780 (2019).
10. Khan, Y. et al. A flexible organic reflectance oximeter array. *Proc. Natl Acad. Sci. USA* **115**, E11015–E11024 (2018).
11. Webb, R. C. et al. Epidermal devices for noninvasive, precise, and continuous mapping of macrovascular and microvascular blood flow. *Sci. Adv.* **1**, e1500701 (2015).
12. Tian, L. et al. Flexible and stretchable 3ω sensors for thermal characterization of human skin. *Adv. Funct. Mater.* **27**, 1701282 (2017).
13. Kim, J., Campbell, A. S., de Ávila, B. E.-F. & Wang, J. Wearable biosensors for healthcare monitoring. *Nat. Biotech.* **37**, 389–406 (2019).
14. Suzuki, D., Oda, S. & Kawano, Y. A flexible and wearable terahertz scanner. *Nat. Photon.* **10**, 809–813 (2016).
15. Garbacz, P. Terahertz imaging—principles, techniques, benefits, and limitations. *J. Mach. Constr. Maint.* **1**, 81–92 (2016).
16. You, B., Chen, C.-Y., Yu, C.-P., Wang, P.-H. & Lu, J.-Y. Frequency-dependent skin penetration depth of terahertz radiation determined by water sorption–desorption. *Opt. Express* **26**, 22709–22721 (2018).
17. Hu, H. et al. Stretchable ultrasonic transducer arrays for three-dimensional imaging on complex surfaces. *Sci. Adv.* **4**, eaar3979 (2018).
18. Wang, C. et al. Monitoring of the central blood pressure waveform via a conformal ultrasonic device. *Nat. Biomed. Eng.* **2**, 687–695 (2018).
19. Schulze, R. K., Ćurić, D. & d'Hoedt, B. B-mode versus A-mode ultrasonographic measurements of mucosal thickness in vivo. *Oral. Surg. Oral. Med. Oral. Pathol. Oral. Radiol. Endod.* **93**, 110–117 (2002).
20. Van Keuk, G. & Blackman, S. S. On phased-array radar tracking and parameter control. *IEEE Trans. Aerosp. Electron. Syst.* **29**, 186–194 (1993).
21. Saucan, A.-A., Chonavel, T., Sintes, C. & Le Caillec, J.-M. CPHD-DOA tracking of multiple extended sonar targets in impulsive environments. *IEEE Trans. Signal Process.* **64**, 1147–1160 (2015).
22. Nissen, S. E. et al. Application of a new phased-array ultrasound imaging catheter in the assessment of vascular dimensions. In vivo comparison to cineangiography. *Circulation* **81**, 660–666 (1990).
23. Baribeau, Y. et al. Hand-held point of care ultrasound probes—the new generation of POCUS. *J. Cardiothorac. Vasc. Anesth.* **34**, 3139–3145 (2020).
24. Cheng, J., Potter, J. N., Croxford, A. J. & Drinkwater, B. W. Monitoring fatigue crack growth using nonlinear ultrasonic phased array imaging. *Smart Mater. Struct.* **26**, 055006 (2017).
25. J. Lee, H.-S. & Sodini, C. G. in *Intracranial Pressure & Neuromonitoring XVI* 111–114 (Springer, 2018).
26. Daum, D. R., Smith, N. B., King, R. & Hynynen, K. In vivo demonstration of noninvasive thermal surgery of the liver and kidney using an ultrasonic phased array. *Ultrasound Med. Biol.* **25**, 1087–1098 (1999).

27. Shi, K., Que, K. & Guo, D. Flexible ultrasonic phased-array probe. *Tsinghua Sci. Technol.* **9**, 574–577 (2004).
28. Bhuyan, A. et al. Miniaturized, wearable, ultrasound probe for on-demand ultrasound screening. In *Proc. IEEE International Ultrasonics Symposium* 1060–1063 (IEEE, 2011).
29. Pashaei, V. et al. Flexible body-conformal ultrasound patches for image-guided neuromodulation. *IEEE Trans. Biomed. Circuits Syst.* **14**, 305–318 (2019).
30. Abdelfattah, R. et al. Outbreak of *Burkholderia cepacia* bacteraemia in a tertiary care centre due to contaminated ultrasound probe gel. *J. Hosp. Infect.* **98**, 289–294 (2018).
31. Thomenius, K. E. Evolution of ultrasound beamformers. In *Proc. IEEE International Ultrasonics Symposium* 1615–1622 (IEEE, 1996).
32. Smith, S. W., Pavy, H. G. & von Ramm, O. T. High-speed ultrasound volumetric imaging system. I. Transducer design and beam steering. *IEEE T. Ultrason. Ferr.* **38**, 100–108 (1991).
33. Gill, R. W. Measurement of blood flow by ultrasound: accuracy and sources of error. *Ultrasound Med. Biol.* **11**, 625–641 (1985).
34. Wooh, S.-C. & Shi, Y. A simulation study of the beam steering characteristics for linear phased arrays. *J. Nondestruct. Eval.* **18**, 39–57 (1999).
35. Cloostermans, M. & Thijssen, J. A beam corrected estimation of the frequency dependent attenuation of biological tissues from backscattered ultrasound. *Ultrason. Imaging* **5**, 136–147 (1983).
36. Ng, A. & Swanevelder, J. Resolution in ultrasound imaging. *Continuing Educ. Anaesthesia Crit. Care Pain* **11**, 186–192 (2011).
37. Gururaja, T. et al. Piezoelectric composite materials for ultrasonic transducer applications. Part I: resonant modes of vibration of PZT rod-polymer composites. *IEEE Trans. Sonics Ultrason.* **32**, 481–498 (1985).
38. Food & Drug Administration *Marketing Clearance of Diagnostic Ultrasound Systems and Transducers* (Center for Devices and Radiological Health, 2019).
39. Gazit, S., Szameit, A., Eldar, Y. C. & Segev, M. Super-resolution and reconstruction of sparse sub-wavelength images. *Opt. Express* **17**, 23920–23946 (2009).
40. Mills, D. M. Medical imaging with capacitive micromachined ultrasound transducer (CMUT) arrays. In *Proc. IEEE Ultrasonics Symposium* 384–390 (IEEE, 2004).
41. Ophir, J., McWhirt, R., Maklad, N. & Jaeger, P. A narrowband pulse-echo technique for in vivo ultrasonic attenuation estimation. In *Proc. IEEE Transactions on Biomedical Engineering* 205–212 (IEEE, 1985).
42. Hunter, A. J., Drinkwater, B. W., Wilcox, P. & Russell, J. Automatic image correction for flexible ultrasonic phased array inspection. In *Proc. 8th International Conference on NDE in Relation to Structural Integrity for Nuclear and Pressurised Components* (JRC-NDE, 2010).
43. Shung, K. K., Sigelmann, R. A. & Reid, J. M. Scattering of ultrasound by blood. In *Proc. IEEE Transactions on Biomedical Engineering* 460–467 (IEEE, 1976).
44. Von Ramm, O. T. & Smith, S. W. Beam steering with linear arrays. In *Proc. IEEE Transactions on Biomedical Engineering* 438–452 (IEEE, 1983).
45. Ketterling, J. A., Aristizabal, O., Turnbull, D. H. & Lizzi, F. L. Design and fabrication of a 40-MHz annular array transducer. *IEEE Trans. Ultrason. Ferroelectr. Freq. Control* **52**, 672–681 (2005).
46. Abbasi, A. S., Chahine, R. A., Mac Alpin, R. N. & Kattus, A. A. Ultrasound in the diagnosis of primary congestive cardiomyopathy. *Chest* **63**, 937–942 (1973).
47. Mohan, J. C. *A Practical Approach to Clinical Echocardiography* (JP Medical, 2014).
48. Ommen, S. R. et al. Clinical utility of Doppler echocardiography and tissue Doppler imaging in the estimation of left ventricular filling pressures: a comparative simultaneous Doppler-catheterization study. *Circulation* **102**, 1788–1794 (2000).
49. Galiuto, L., Ignone, G. & DeMaria, A. N. Contraction and relaxation velocities of the normal left ventricle using pulsed-wave tissue Doppler echocardiography. *J. Am. Coll. Cardiol.* **81**, 609–614 (1998).
50. Søgaard, P. et al. Tissue Doppler imaging predicts improved systolic performance and reversed left ventricular remodeling during long-term cardiac resynchronization therapy. *Am. J. Cardiol.* **40**, 723–730 (2002).
51. Auricchio, A. et al. Long-term clinical effect of hemodynamically optimized cardiac resynchronization therapy in patients with heart failure and ventricular conduction delay. *Am. J. Cardiol.* **39**, 2026–2033 (2002).
52. Auricchio, A. & Abraham, W. T. Cardiac resynchronization therapy: current state of the art: cost versus benefit. *Circulation* **109**, 300–307 (2004).
53. Thimot, J. & Shepard, K. L. Bioelectronic devices: wirelessly powered implants. *Nat. Biomed. Eng.* **1**, 0051 (2017).
54. Joyner, C. R. Jr, Hey, E. B. Jr, Johnson, J. & Reid, J. M. Reflected ultrasound in the diagnosis of tricuspid stenosis. *Am. J. Cardiol.* **19**, 66–73 (1967).
55. Flammer, A. J. et al. The assessment of endothelial function: from research into clinical practice. *Circulation* **126**, 753–767 (2012).
56. Petrofsky, J. S. Resting blood flow in the skin: does it exist, and what is the influence of temperature, aging, and diabetes? *J. Diabetes Sci. Technol.* **6**, 674–685 (2012).
57. Herholz, K. et al. Regional cerebral blood flow in patients with leuko-araiosis and atherosclerotic carotid artery disease. *Arch. Neurol.* **47**, 392–396 (1990).
58. Boutry, C. M. et al. Biodegradable and flexible arterial-pulse sensor for the wireless monitoring of blood flow. *Nat. Biomed. Eng.* **3**, 47–57 (2019).
59. Dymling, S. O., Persson, H. W. & Hertz, C. H. Measurement of blood perfusion in tissue using Doppler ultrasound. *Ultrasound Med. Bio.* **17**, 433–444 (1991).
60. Chung, C. P. et al. More severe white matter changes in the elderly with jugular venous reflux. *Ann. Neurol.* **69**, 553–559 (2011).
61. Merritt, C. R. Doppler colour flow imaging. *J. Clin. Ultrasound* **15**, 591–597 (1987).
62. Bland, J. M. & Altman, D. Statistical methods for assessing agreement between two methods of clinical measurement. *Lancet* **327**, 307–310 (1986).
63. Bondar, R. L. et al. Cerebral blood flow velocities by transcranial Doppler during parabolic flight. *J. Clin. Pharmacol.* **31**, 915–919 (1991).
64. Jawad, K., Miller, J. D., Wyper, D. J. & Rowan, J. O. Measurement of CBF and carotid artery pressure compared with cerebral angiography in assessing collateral blood supply after carotid ligation. *J. Neurosurg.* **46**, 185–196 (1977).
65. Cope, M. & Delpy, D. T. System for long-term measurement of cerebral blood and tissue oxygenation on newborn infants by near infra-red transillumination. *Med. Biol. Eng. Comput.* **26**, 289–294 (1988).
66. Soustiel, J. et al. Assessment of cerebral blood flow by means of blood-flow-volume measurement in the internal carotid artery: comparative study with a 133xenon clearance technique. *Stroke* **34**, 1876–1880 (2003).
67. Gunst, M. et al. Accuracy of cardiac function and volume status estimates using the bedside echocardiographic assessment in trauma/critical care. *J. Trauma Acute Care Surg.* **65**, 509–516 (2008).
68. Podstawski, R., Kasietczuk, B., Boraczyński, T., Boraczyński, M. & Choszcz, D. Relationship between BMI and endurance-strength abilities assessed by the 3 minute burpee test. *Int. J. Sports Sci.* **3**, 28–35 (2013).
69. Ma, Y.-C., Peng, C.-T., Huang, Y.-C., Lin, H.-Y. & Lin, J.-G.The depths from skin to the major organs at chest acupoints of pediatric patients. *Evid. Based Complement. Altern. Med.* **2015**, 126028 (2015).
70. Huang, Z. et al. Three-dimensional integrated stretchable electronics. *Nat. Electron.* **1**, 473–480 (2018).
71. Burckhardt, C. B. Speckle in ultrasound B-mode scans. *IEEE Trans. Sonics Ultrason.* **25**, 1–6 (1978).
72. Liu, Y. et al. Epidermal mechano-acoustic sensing electronics for cardiovascular diagnostics and human-machine interfaces. *Sci. Adv.* **2**, e1601185 (2016).
73. Delgado-Trejos, E., Quiceno-Manrique, A., Godino-Llorente, J., Blanco-Velasco, M. & Castellanos Dominguez, G. Digital auscultation analysis for heart murmur detection. *Ann. Biomed. Eng.* **37**, 337–353 (2009).
74. Lee, K. et al. Mechano-acoustic sensing of physiological processes and body motions via a soft wireless device placed at the suprasternal notch. *Nat. Biomed. Eng.* **4**, 148–158 (2019).

Acknowledgements

We thank Z. Wu and L. Chen for guidance on the ultrasonic imaging algorithm and data processing; S. Xiang for feedback on manuscript preparation; and Y. Hu and Z. Liu for advice on the cardiac tissue Doppler experiments. The content is solely the responsibility of the authors and does not necessarily represent the official views of the National Institutes of Health (NIH). All biological experiments were conducted in accordance with the ethical guidelines of the NIH and with the approval of the IRB of the University of California, San Diego (IRB number 170812). We acknowledge support from the NIH (grant 1R21EB027303-01A1) and the Center for Wearable Sensors at the University of California, San Diego.

Author contributions

C.W., B.Q., M.L., Z.Z. and S.X. designed the research. C.W., B.Q., M.L., B.L. and Z.Z. performed the experiments. C.W., B.Q. and Z.Z. performed the simulations. C.W., Z.Z., B.Q. and M.L. analysed the data. C.W. and S.X. wrote the paper. All authors provided active and valuable feedback on the manuscript.

Competing interests

The authors declare no competing interests.

Additional information

Extended data is available for this paper at https://doi.org/10.1038/s41551-021-00763-4.

Supplementary information The online version contains supplementary material available at https://doi.org/10.1038/s41551-021-00763-4.

Correspondence and requests for materials should be addressed to S.X.

Peer review information *Nature Biomedical Engineering* thanks John Ho and the other, anonymous, reviewer(s) for their contribution to the peer review of this work.

Reprints and permissions information is available at www.nature.com/reprints.

Publisher's note Springer Nature remains neutral with regard to jurisdictional claims in published maps and institutional affiliations.

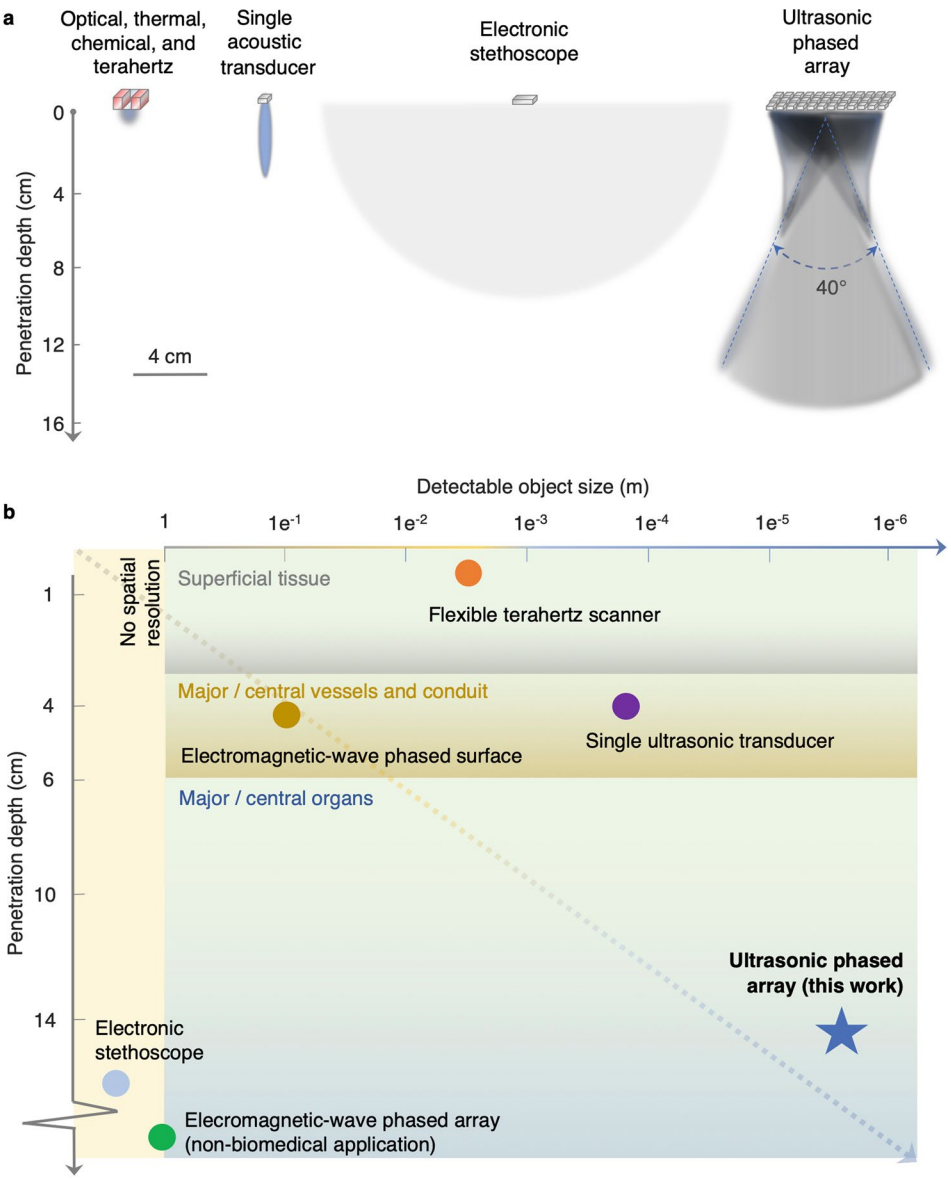

Extended Data Fig. 1 | Comparison of existing flexible or stretchable electronic devices for deep-tissue monitoring. a, Comparison of the detection range (shaded areas underneath each sensing mode) of the stretchable phased array with all other flexible/stretchable biosensors, including optoelectronics, thermal electronics, iontophoresis based electrochemical sensors, terahertz wave-based sensors, a single ultrasonic transducer, and electronic stethoscopes. The phased array has distinct advantages compared to the other sensing modalities in both penetration depth and spatial resolution. With phased array beamforming, the stretchable ultrasonic probe can focus the beam to achieve longer penetration (up to 14 cm in human tissues) and steer the beam to scan over a 40° range with a high signal-to-noise ratio (SNR). The insonation area in 2D can reach ~68.41 cm^2, 380 times larger than the insonation area of a single element, ~0.18 cm^2, calculated by Field II, MATLAB, MathWorks, Natick, MA. **b**, Comparison of the penetration depth and detectable object size of representative flexible/stretchable biosensors in the literature. Stretchable optoelectronics illuminates the tissue to analyze changes in blood oxygen saturation, but the depth of penetration is generally limited to ~8 mm[8–10]. Stretchable thermal electronics suffer from similar limitations[11,12]. Although flexible terahertz devices show high penetration in dielectric materials[14], terahertz electromagnetic waves attenuate quickly in water[15], leading to a maximum penetration depth of only 0.3 mm in the human tissue[16]. Flexible electromagnetic devices in the frequency range of ~GHz can penetrate more than 5 cm of human tissue, but their spatial resolution ranges from 5 to 50 cm, which is inadequate for most biomedical applications[4]. Stretchable stethoscopes based on kinematics can sense vibrations far beneath the skin[72]; but due to the omnidirectional propagation of vibrations, these devices can receive signals from all organs in their sensing range, and thus lack spatial resolution[73,74]. Additionally, they can only detect low-frequency pulsations, missing critical information from static objects (for example, their location, dimension, and modulus) or high-frequency pulsations (for example, hemodynamics). The result shows the stretchable phased array has a long penetration depth with sufficient resolving capabilities for deep tissue monitoring.

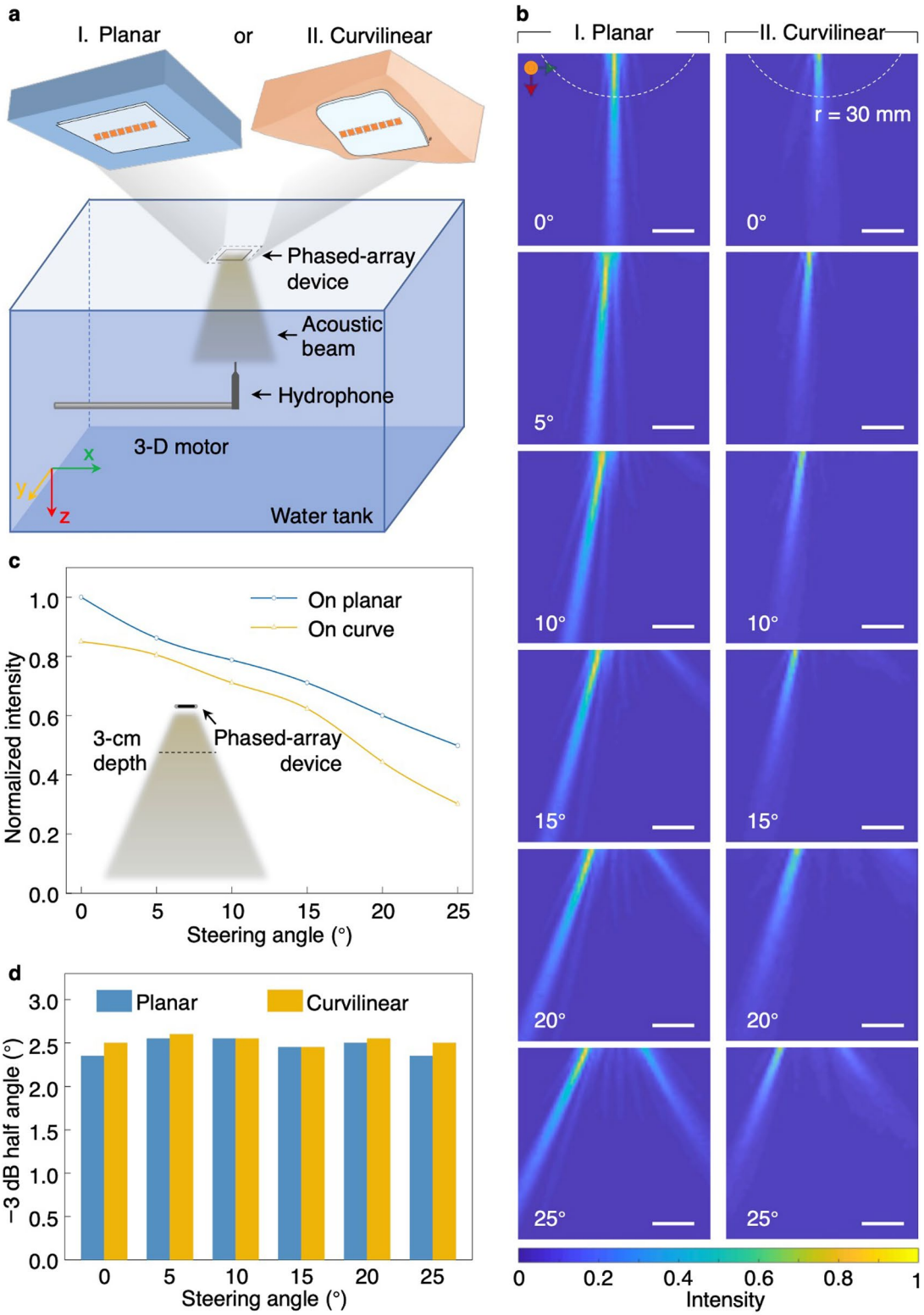

Extended Data Fig. 2 | Performance of the stretchable phased array at all incidence angles in the *xz* plane on the phantom replicated from the human neck. a, A schematic setup of the characterization. Ultrasonic field mapping is carried out with the stretchable phased array on a flat (top left) or a curvilinear (top right) surface. The characterization system is composed of a water tank and a 3D motor system with a hydrophone at its tip. **b**, Mapped ultrasonic fields with the stretchable phased array on a flat (left) or a curvilinear (right) surface with an incidence angle range of 0° - 25°. Scale bars are 2 cm. **c**, Normalized beam intensity of the stretchable phased array at a typical carotid artery depth (~3 cm) with different incident angles. The inset illustrates the depth at which the intensity measurements are taken. **d**, Beam directivity of the stretchable phased array at a typical carotid artery depth (~3 cm) with different incident angles. The beam directivity of the stretchable phased array is comparable on the two surfaces at all incident angles in the range tested.

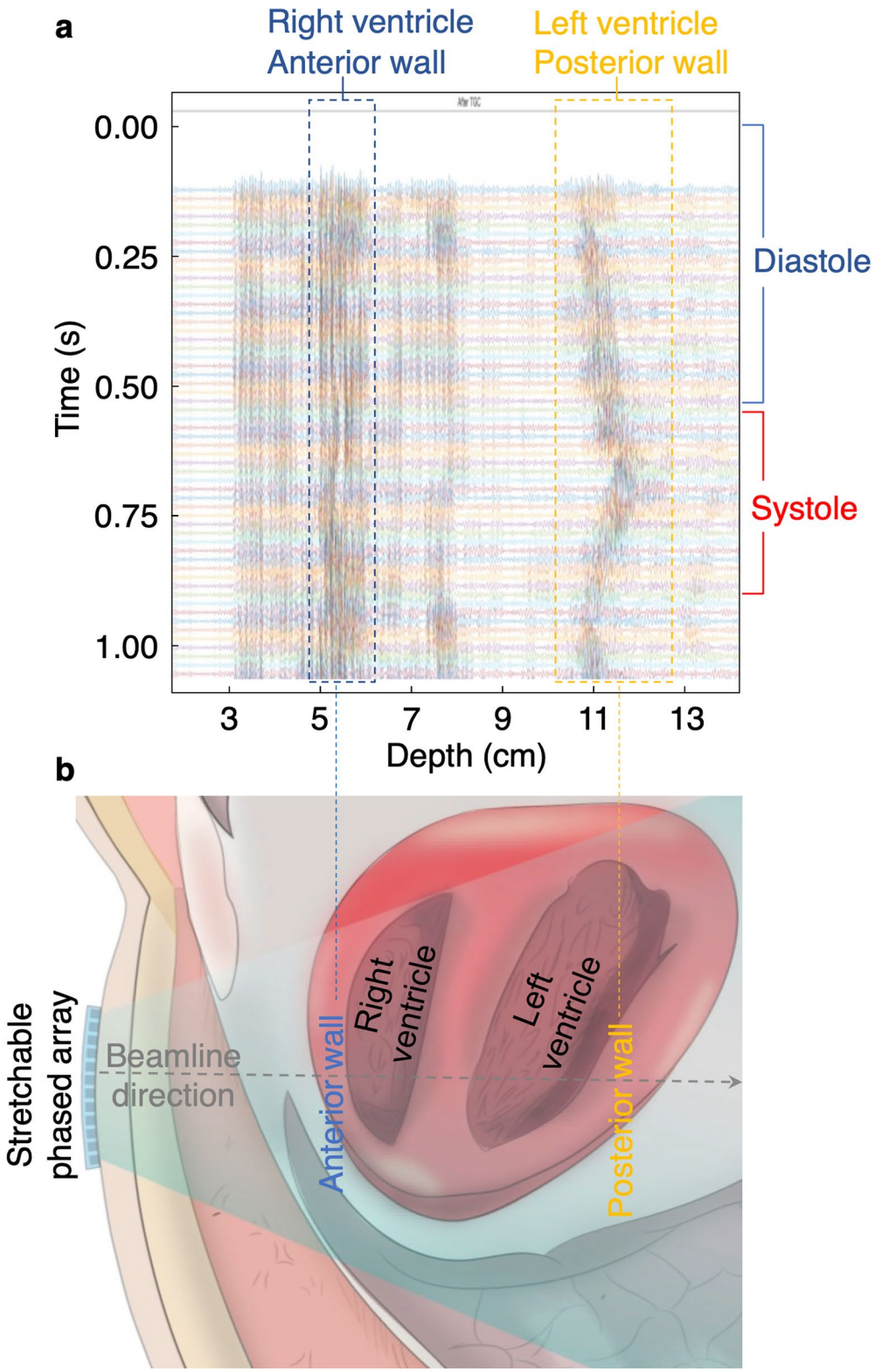

Extended Data Fig. 3 | Raw radiofrequency signals of the tissue Doppler in the time domain, and corresponding human anatomy. a, Raw radiofrequency signals of the tissue Doppler in one cardiac cycle. Note that the y-axis is time. The x-axis is converted to depth by multiplying the ultrasonic speed by the time-of-flight of ultrasonic pulses in the human tissue. As a proof of concept, we neglect the non-uniformity of the ultrasonic speed in the human body. From the pattern, we can clearly observe the reflection peaks from the anterior wall of the right ventricle (RV) in the blue dashed box and the posterior wall of the left ventricle (LV) in the orange dashed box. The positions of the reflection peaks shift during the cardiac cycle. The RV anterior wall peak shifts to the left from 0 to 0.6 s, corresponding to RV diastole, and shifts to the right from 0.6 to 0.8 s, corresponding to RV systole. Meanwhile, the LV posterior wall peak shifts to the right from 0 to 0.6 s, corresponding to LV diastole, and shifts to the left from 0.6 to 0.8 s, corresponding to LV systole. The peak shifting clearly indicates the relaxation and contraction of the cardiac chambers. **b**, The cross-sectional structure of the parasternal short-axis view corresponding to the signal peaks in a.

nature research

Corresponding author(s): Sheng Xu

Last updated by author(s): May 28, 2021

Reporting Summary

Nature Research wishes to improve the reproducibility of the work that we publish. This form provides structure for consistency and transparency in reporting. For further information on Nature Research policies, see our Editorial Policies and the Editorial Policy Checklist.

Statistics

For all statistical analyses, confirm that the following items are present in the figure legend, table legend, main text, or Methods section.

n/a	Confirmed	
☐	☒	The exact sample size (*n*) for each experimental group/condition, given as a discrete number and unit of measurement
☐	☒	A statement on whether measurements were taken from distinct samples or whether the same sample was measured repeatedly
☐	☒	The statistical test(s) used AND whether they are one- or two-sided *Only common tests should be described solely by name; describe more complex techniques in the Methods section.*
☒	☐	A description of all covariates tested
☒	☐	A description of any assumptions or corrections, such as tests of normality and adjustment for multiple comparisons
☐	☒	A full description of the statistical parameters including central tendency (e.g. means) or other basic estimates (e.g. regression coefficient) AND variation (e.g. standard deviation) or associated estimates of uncertainty (e.g. confidence intervals)
☐	☒	For null hypothesis testing, the test statistic (e.g. *F*, *t*, *r*) with confidence intervals, effect sizes, degrees of freedom and *P* value noted *Give P values as exact values whenever suitable.*
☒	☐	For Bayesian analysis, information on the choice of priors and Markov chain Monte Carlo settings
☐	☒	For hierarchical and complex designs, identification of the appropriate level for tests and full reporting of outcomes
☒	☐	Estimates of effect sizes (e.g. Cohen's *d*, Pearson's *r*), indicating how they were calculated

Our web collection on statistics for biologists contains articles on many of the points above.

Software and code

Policy information about availability of computer code

Data collection	Data collection of the ultrasound signal was carrried out with the Verasonics Vantage platform.
Data analysis	Data of the ultrasound signal was analyzed via the Verasonics Vantage and Matlab platform.

For manuscripts utilizing custom algorithms or software that are central to the research but not yet described in published literature, software must be made available to editors and reviewers. We strongly encourage code deposition in a community repository (e.g. GitHub). See the Nature Research guidelines for submitting code & software for further information.

Data

Policy information about availability of data

All manuscripts must include a data availability statement. This statement should provide the following information, where applicable:

- Accession codes, unique identifiers, or web links for publicly available datasets
- A list of figures that have associated raw data
- A description of any restrictions on data availability

The main data supporting the results in this study are available within the paper and its Supplementary Information. Data generated in this study, including source data and the data used to make the figures, are available from Harvard Dataverse via the identifier https://dataverse.harvard.edu/dataset.xhtml?persistentId=doi:10.7910/DVN/EPITIY.

Field-specific reporting

Please select the one below that is the best fit for your research. If you are not sure, read the appropriate sections before making your selection.

☒ Life sciences ☐ Behavioural & social sciences ☐ Ecological, evolutionary & environmental sciences

For a reference copy of the document with all sections, see nature.com/documents/nr-reporting-summary-flat.pdf

Life sciences study design

All studies must disclose on these points even when the disclosure is negative.

Sample size	Three healthy subjects, for proof-of-principle testing.
Data exclusions	No data were excluded.
Replication	All attempts at data replication were successful.
Randomization	Not relevant. Validation testing was carried out as a correlation analysis between the newly developed prototype and a standard tool.
Blinding	Not relevant.

Reporting for specific materials, systems and methods

We require information from authors about some types of materials, experimental systems and methods used in many studies. Here, indicate whether each material, system or method listed is relevant to your study. If you are not sure if a list item applies to your research, read the appropriate section before selecting a response.

Materials & experimental systems

n/a	Involved in the study
☒	☐ Antibodies
☒	☐ Eukaryotic cell lines
☒	☐ Palaeontology and archaeology
☒	☐ Animals and other organisms
☐	☒ Human research participants
☒	☐ Clinical data
☒	☐ Dual use research of concern

Methods

n/a	Involved in the study
☒	☐ ChIP-seq
☒	☐ Flow cytometry
☒	☐ MRI-based neuroimaging

Human research participants

Policy information about studies involving human research participants

Population characteristics	Blood flow was measured on three healthy subjects in a static sitting position.
Recruitment	All human-testing subjects participating in blood flow measurements and skin-curvature characterizations had all agreed to the voluntary consent.
Ethics oversight	All experiments were conducted in accordance with the ethical guidelines of the NIH and with the approval of the Institutional Review Board of the University of California, San Diego (IRB no. 170812).

Note that full information on the approval of the study protocol must also be provided in the manuscript.